

Favorable property integration in high entropy alloys via dissimilar friction stir welding: a case study using Al_{0.3}CoCrFeNi and Fe_{38.5}Co₂₀Mn₂₀Cr₁₅Si₅Cu_{1.5} HEAs

Ravi Sankar Haridas^{a,c,d,*}, Anurag Gumaste^{b,c}, Priyanshi Agrawal^{b,c,1}, Surekha Yadav^{b,c,2}, Rajiv S. Mishra^{b,c,d,**}

^a Department of Mechanical Engineering, University of North Texas, Denton, TX 76207, USA

^b Department of Materials Science and Engineering, University of North Texas, Denton, TX 76207, USA

^c Center for Friction Stir Processing, University of North Texas, Denton, TX 76207, USA

^d Advanced Materials and Manufacturing Processes Institute, University of North Texas, Denton, TX 76207, USA

*Corresponding author e-mail: Ravisankar.Haridas@unt.edu

**Corresponding author e-mail: Rajiv.Mishra@unt.edu

Abstract:

The advent of high entropy alloys (HEAs) enabled fine-tuning of the alloy composition from the vast compositional space to develop solid-solution alloys having good physical and mechanical properties. Each HEA composition is the culmination of careful alloy design strategy aimed at a specific property intended for a specific application that is achieved by microstructural alteration and/or activation of deformation mechanisms. Methods to integrate the favorable properties pertaining to each HEA potentially benefit alloy selection for structural applications. In this study, dissimilar friction stir welding (FSW) was performed using Al_{0.3}CoCrFeNi HEA and Fe_{38.5}Co₂₀Mn₂₀Cr₁₅Si₅Cu_{1.5} TRIP HEA to integrate the beneficial mechanical properties of both HEAs. Unlike fusion welding methods that lead to a weaker weld zone, dissimilar FSW of the HEAs resulted in a refined microstructure in the stir zone (SZ) with enhanced mechanical performance compared to both base materials and enabled promising property integration. Improved and integrated mechanical property achieved in SZ was correlated to the microstructure, existing recrystallization mechanisms, and active deformation mechanisms in both alloys.

¹ Current address: Materials Science and Technology Division, Oak Ridge National Laboratory, Oak Ridge, TN, USA.

² Current address: Edison Welding Institute, Columbus, Ohio, 43221.

Keywords: Dissimilar friction stir welding; high entropy alloys; dynamic recrystallization; martensitic transformation; mechanical property

1 Introduction

Development of high entropy alloys (HEAs) enabled single-phase solid solutions in multi-component alloy systems by virtue of high entropy of mixing of constituent elements, thereby eliminating the presence of any secondary phases [1]. The possibility of exploring the vast compositional space led to the discovery of HEA compositions with synergy of excellent strength and ductility, fracture toughness, oxidation and corrosion resistance, fatigue and wear resistance, as well as high-temperature properties [2]. Such an ability to design the HEAs for property- and design-specific applications makes them potential next-generation candidates for structural applications.

Metal joining is an inevitable part of the structural fabrication process line that demands thorough investigation for each alloy class. Understanding the processability of a new class of alloys is inevitable to qualify the alloy for structural applications. Since welding is a major joining process used in structural fabrication, understanding the weldability of HEAs is of prime interest. Guo et al. [3] were the first to gather the available information on welding of HEAs and provided insights into the weld performance as a function of alloy composition and weld method. In their review, Lopes and Oliveira [4] provided a brief outlook on weldability of the most-explored CoCrFeMnNi HEA and Al_xCoCrFeNi HEA systems. Remarkable mechanical performance achieved in solid-state welding over fusion welding was emphasized. Li et al. [5] extensively reviewed the recent trends in both fusion welding and solid-state welding of HEAs and expressed lack of a comprehensive knowledge on the challenges faced during welding of HEAs. Additionally, the possibility of realizing the potential of weld joints with property integration for multi-functional application was proposed. Dissimilar welding of different HEAs to achieve favorable property integration could be one such aspect. Judicious selection of HEAs from its vast pool for such property integration is recommended for optimum results. Also, the ability to achieve a sound weld of dissimilar HEAs needs to be investigated. Dissimilar fusion welding of HEAs with conventional alloys such as stainless steels [6,7], INCONEL 718 [8], and aluminum [9] was tried in an attempt to explore the feasibility of achieving a sound weld. Gas tungsten arc welding of Al_{0.1}CoCrFeNi HEA with INCONEL 718 resulted in an inferior weld

mechanical property as compared to both base materials [8]. Similar weld property reduction was also observed in dissimilar laser welding of CoCrFeMnNi HEA with a duplex stainless steel [10]. Oliveira et al. [6] attempted dissimilar welding of CoCrFEMnNi HEA with SS316; and the mechanical response of the weld showed strength and ductility values less than the respective base material. Although altering the microstructure of the base material improved ductility [11], the values were still less than the base material counterparts.

Although the concept of HEAs started with the notion of achieving a single-phase solid solution via equiatomic mixing of multiple elements [12], the desire to expand the mechanical performance of HEAs led to the evolution of multi-elemental alloy systems that, unlike equiatomic HEAs, occupy slightly off-center positions in the phase diagram. Such alloys used either deformation-induced martensitic transformation [13] or precipitation strengthening [14] to improve their mechanical performance, and termed as complex concentrated alloys (CCAs). Al_{0.3}CoCrFeNi HEA (Al_{0.3} HEA) was reported to show a wide range of mechanical properties by virtue of microstructure tunability due to the existence of a rich phase field with temperature variation [15]. The fcc-single-phase microstructure of Al_{0.3}-HEA showed excellent uniform ductility (>60%) as well as non-uniform ductility post-necking, although low in strength. Strength of the same alloy could be improved by an enormous 1000% by using Hall-Petch strengthening and precipitation strengthening [16,17]. Additionally, the alloy exhibited good fatigue property [18] and impact resistance [19]. Similarly, another Fe_{38.5}Co₂₀Mn₂₀Cr₁₅Si₅Cu_{1.5} TRIP HEA (Cu_{1.5} HEA) enabled good strength and work hardenability owing to persistent γ (f.c.c.) $\rightarrow\epsilon$ (h.c.p) martensitic transformation [20]. The alloy also showed exceptional fatigue resistance in its fine-grained microstructure [21] and good corrosion resistance as well. Cu addition to FeCoCrMnSi alloy system improved the stability of the high-temperature γ (f.c.c.) phase upon thermomechanical processing, thereby yielding larger volume fraction of γ (f.c.c.) available for deformation induced transformation. Higher volume fraction of the γ (f.c.c.) phase resulted in good strength and excellent work hardening under tensile deformation [20]. Hence, methods to integrate the flexibility in mechanical property tuning by utilizing the richness of phase field available in Al_{0.3} HEA and work hardening in Cu_{1.5} HEA owing to its capability of martensitic transformation would be beneficial for structural applications.

Unlike fusion welding of HEAs, which resulted in a weaker weld zone, solid-state friction stir welding (FSW) was reported to improve the mechanical property of the weld zone in various HEAs such as CoCrFeMnNi [22], carbon-doped CoCrFeMnNi [23], CoCrFeNi [24], Al_{0.3}CoCrCu_{0.3}FeNi [25], Fe₄₉Mn₃₀Cr₁₀Co₁₀C₁ [26], Al_{0.3}CoCrFeNi [27], and Fe_{38.5}Co₂₀Mn₂₀Cr₁₅Si₅Cu_{1.5} [20]. The stir zone (SZ) showed a refined microstructure following dynamic recrystallization, which is typical in FSW. The present study is an attempt of dissimilar FSW of Al_{0.3} HEA and Cu_{1.5} HEA to check the viability of achieving a sound weld with the intention of integrating the favorable mechanical properties of both alloys. Detailed microstructural and mechanical characterization was performed for weld quality qualification. Additionally, the recrystallization mechanism pertaining to both alloys and the active deformation mechanisms were investigated.

2 Materials

The HEAs considered for dissimilar welding were Al_{0.3} HEA and Cu_{1.5} HEA. The HEAs considered for the study are produced by vacuum arc-casting in a cold copper crucible by melting 99.9% pure elements. Homogenization is achieved by multiple flips and re-melting cycles. Nominal and actual composition of both alloys is provided in Table 1. Al_{0.3} HEA was further hot-rolled to quarter-inch thickness (*t*) followed by heat treatment at 620°C for 100 hours to obtain a partially recrystallized microstructure. Similarly, Cu_{1.5} HEA was also hot-rolled to quarter inch thickness.

Table 1: Elemental composition of cast ingot of Al_{0.3}-HEA and Cu_{1.5}-HEA.

Alloy	Composition (at.%)	Fe	Mn	Co	Cr	Ni	Si	Cu	Al
Cu _{1.5} HEA	Nominal	38.5	20	20	15	-	5	1.5	-
	Actual	38.9 4	20.1 3	20.4 5	14.2 8	-	4.81	1.58	-
Al _{0.3} HEA	Nominal	23.2 6	-	23.2 6	23.2 6	23.2 6	-	-	6.98
	Actual	22.3 8	-	23.6 7	23.3 1	23.8 2	-	-	6.81

3 Methods

The quarter-inch rolled plates of Al_{0.3}-HEA and Cu_{1.5}-HEA were cut into plates having dimensions 6" length (L) and 3" width (W). The abutting edges of both plates were milled using a Tormach® PCNC 440 CNC milling machine to minimize surface irregularities and achieve close contact between the abutting edges. FSW was performed on a Manufacturing Technology, Inc. welding machine. The parameters used for FSW are given in Table 2. The parameters were based on the authors' experience on FSW of HEAs over last 7 years [28]. A W-Re tool having the dimensions shown in Fig. 1 (b) was used for the welding. Additionally, a tool tilt angle was provided to generate an additional downward thrust during traverse on the hot plasticized material to avoid the possibility of worm hole defect formation. A schematic of FSW of dissimilar welding of Al_{0.3}-HEA and Cu_{1.5}-HEA is shown in Fig. 1. Cu_{1.5}-HEA was placed on the advancing side (AS) and Al_{0.3}-HEA was placed on the retreating side (RS) of the weld run. The position of the plates was decided based on previous reports on ductility and work hardening of both HEAs [19,20]. Cu_{1.5} HEA being more ductile when compared to Al_{0.3} HEA was placed on the AS to facilitate better material flow from AS to RS around the tool, to achieve excellent bonding along the weld line. Further, Argon gas supply was provided over the weld during the run to minimize oxygen contamination during the process.

Table 2: FSW parameters used for the dissimilar HEA welding.

Rotational speed	150 RPM
Plunge speed	1 IPM
Traverse speed	2 IPM
Tool tilt angle	2.5°
Plunge depth	4.1 mm

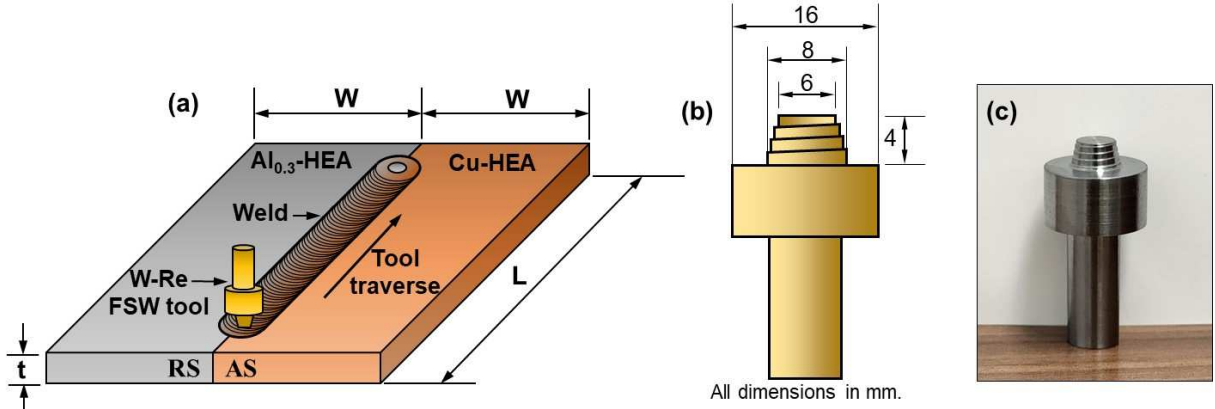


Figure 1: (a) Schematic of dissimilar FSW of Cu_{1.5}-HEA and Al_{0.3}-HEA, (b) schematic of the W-Re tool used for FSW indicating the significant dimensions, and (c) W-Re tool used for FSW.

Mini-tensile samples were milled out from the base materials and weld to determine location-specific mechanical property of the weld. Mini-tensile samples having dimensions 5 mm gage length and 1.25 × 1.25 mm² cross section were milled out using Tormach® PCNC 440 CNC milling machine. A custom-made mini-tensile testing machine equipped with 2 kN load cell and LVDT was used to conduct mini-tensile tests. All tests were performed at an initial strain rate of 10⁻³ s⁻¹. Mini-tensile samples were polished up to a surface finish of 1200 (P-4000) SiC grit paper before test to minimize surface undulations. Schematics of the mini-tensile sample locations machined from the base materials and weld zone are indicated in Fig. 2. Samples A and D correspond to the base material of Al_{0.3}-HEA and Cu_{1.5}-HEA, respectively. Similarly, samples B and C were milled out from the weld zone such that the gage volume was confined to the processed zones of Al_{0.3}-HEA and Cu_{1.5}-HEA, respectively, to determine the mechanical property of the processed zone of individual HEAs. Sample E was machined out from the weld zone to include both processed alloys in the gage section to determine weld strength and weld efficiency across the weld line. Additionally, a tensile test was performed on a sub-sized ASTM E8 [29] sample extracted across the weld (Fig. 2). Gage volume of the tensile sample includes both base materials and weld zone. In addition to weld strength determination, a tensile test on such a sample enables understanding the progression of deformation at different zones during the tensile test. The sub-sized ASTM E8 sample was prepared on a Kent Industries USA Inc. WSi-200 wire-EDM machine. The sample was polished on 1200 SiC grit paper to remove the surface oxides as well as to remove any surface irregularities. The test was conducted on an MTS 322 load frame equipped with 500 kN load cell at an initial strain rate of 10⁻³ s⁻¹. Digital image

correlation (DIC) was performed to obtain strain mapping during the tensile test using the hardware from Correlated Solutions, Inc. A speckled pattern was applied on the sample surface, and the images for DIC were captured at a frequency of 5 Hz using Vic-Gauge 2D real-time strain monitoring software. The images were further analyzed using Vic 2D software to obtain *in situ* strain mapping. Micro-hardness was measured using Buehler Wilson VH3300 auto hardness tester at a test load of 100 gf, 10 sec dwell time, and 500 μm indent spacing.

Samples for microscopy and micro hardness measurement were polished to 0.02 μm colloidal silica solution followed by vibratory polishing for 24 hours in Buehler VibroMet 2 polisher. Electron back scattered diffraction (EBSD) and energy dispersive X-ray spectroscopy (EDS) analysis were performed on FEI Nova NanoSEM 230 equipped with Hikari super EBSD detector functioning at operating voltage of 20 kV and spot size of 6. The sample was held on a 70° pre-tilted stub, and the EBSD scans were acquired using TEAM™ software at a step size of 0.35 μm . Further analysis of the EBSD data was achieved using TSL OIM 8 software. Fractography of the failed samples was performed on FEI Quanta 200 ESEM.

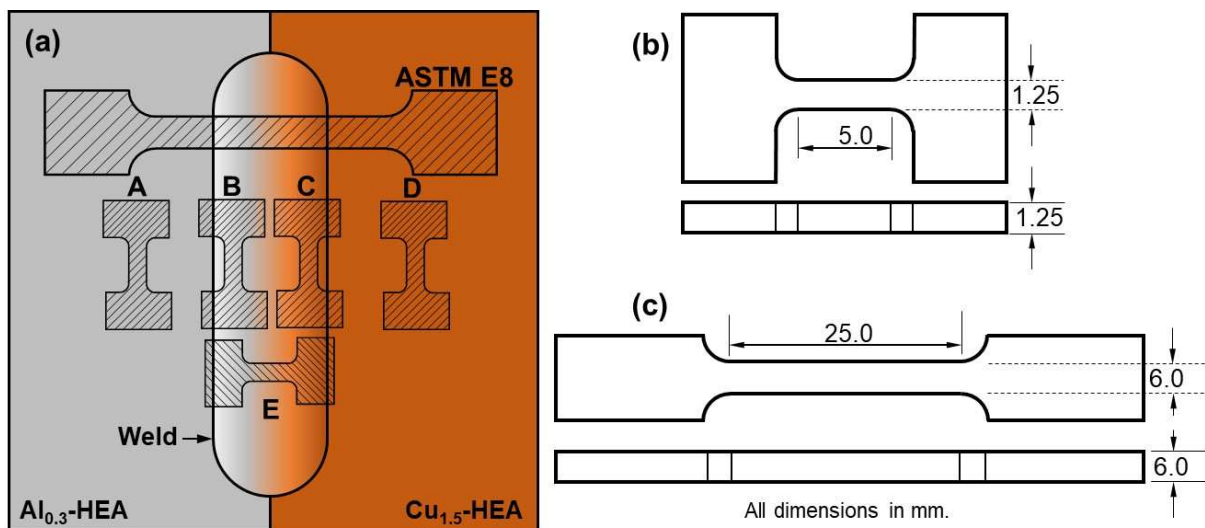


Figure 2: Schematic of the location of mini-tensile samples and sub-sized ASTM E8 sample extracted from the dissimilar weld, (b) schematic of the mini-tensile sample indicating significant dimensions, and (c) schematic of sub-sized ASTM E8 sample indicating significant dimensions.

4 Results

4.1 Microstructure

Inverse pole figure (IPF) maps at different locations of the dissimilar weld marked by different colored boxes (Fig. 3 schematic) indicate microstructural variation across the weld. The base material of $\text{Al}_{0.3}$ HEA after hot-rolling resulted in a partially recrystallized microstructure with fine recrystallized grains surrounding the periphery of the larger elongated grains and a concomitant necklace microstructure (Fig. 3 (a)). The microstructure is comprised of single-phase γ (f.c.c.) as revealed by the phase map (Fig. 4 (a)). However, the initial microstructure of hot-rolled $\text{Cu}_{1.5}$ HEA (Fig. 3 (b)) showed an equiaxed morphology ($18.62 \pm 14.22 \mu\text{m}$) with a dual phase microstructure that consisted of metastable γ (f.c.c.) and ε (h.c.p) martensitic phases; 82.4% γ (f.c.c.) and 17.6% ε (h.c.p) (Fig. 4 (b)).

Dissimilar FSW of both HEAs resulted in severe grain refinement in the weld zone. Figures 3 (c) and 3 (d) show the transition in grain morphology from the unprocessed zone to the processed zone at the $\text{Cu}_{1.5}$ HEA side and $\text{Al}_{0.3}$ HEA side, respectively; and reveal the level of grain refinement achieved after FSW. The material in the processed zone undergoes shear deformation at high strain rate and temperature due to the rotational and translational motion of the FSW tool. During the process, which culminates in the final fine-grained recrystallized microstructure, the alloy in the stir zone (SZ) undergoes multiple dynamic recrystallization and grain growth cycles due to continuous shearing of the material by the FSW tool. Figures 3 (d) and 3 (f) show the final microstructure of $\text{Cu}_{1.5}$ HEA and $\text{Al}_{0.3}$ HEA at their respective locations in the SZ (location D and F) as indicated in the schematic. Average grain size for $\text{Al}_{0.3}$ HEA was $1.98 \pm 1.63 \mu\text{m}$, whereas that for $\text{Cu}_{1.5}$ HEA was $2.45 \pm 2.03 \mu\text{m}$. Variation in grain refinement in both alloys could be due to multiple reasons; variation in (i) starting microstructure, (ii) stick-slip coefficient between the rotating tool and individual work pieces, (iii) coefficient of friction between the tool and individual work pieces, (iv) position of the work piece with respect to the direction of tool traverse, and (v) mechanism of dynamic recrystallization.

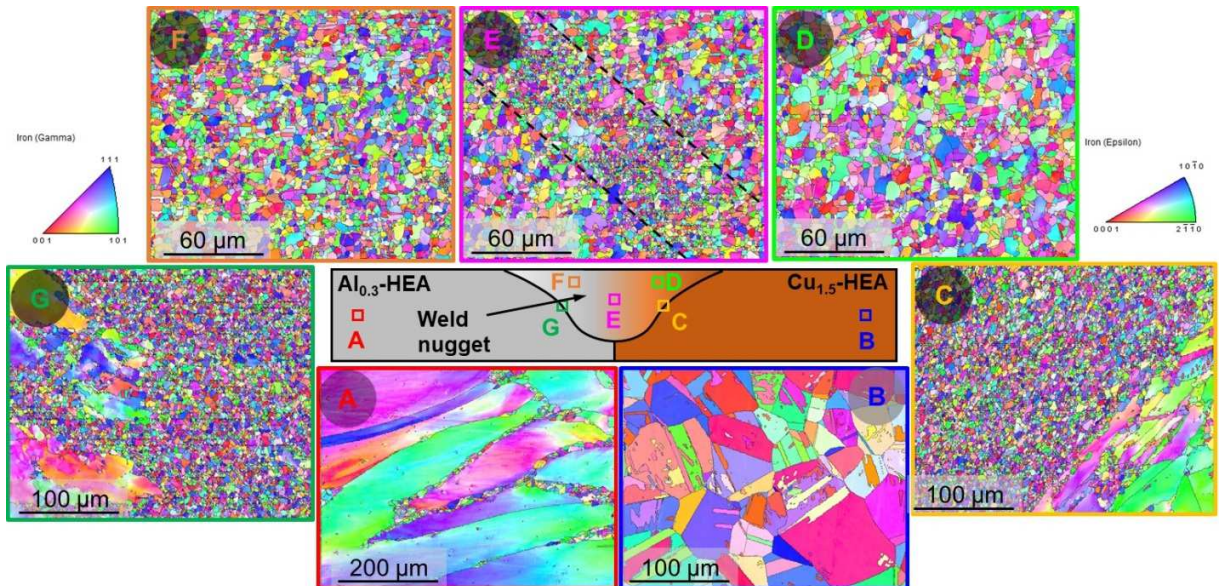


Figure 3: Inverse pole figure (IPF) maps obtained at multiple locations along the dissimilar weld of Al_{0.3} HEA and Cu_{1.5} HEA. (a) Base Al_{0.3} HEA, (b) base Cu_{1.5} HEA, (c) transition zone Al_{0.3} HEA, (d) SZ Cu_{1.5} HEA, (e) dissimilar weld line, (f) SZ Al_{0.3} HEA, and (g) transition zone Al_{0.3} HEA.

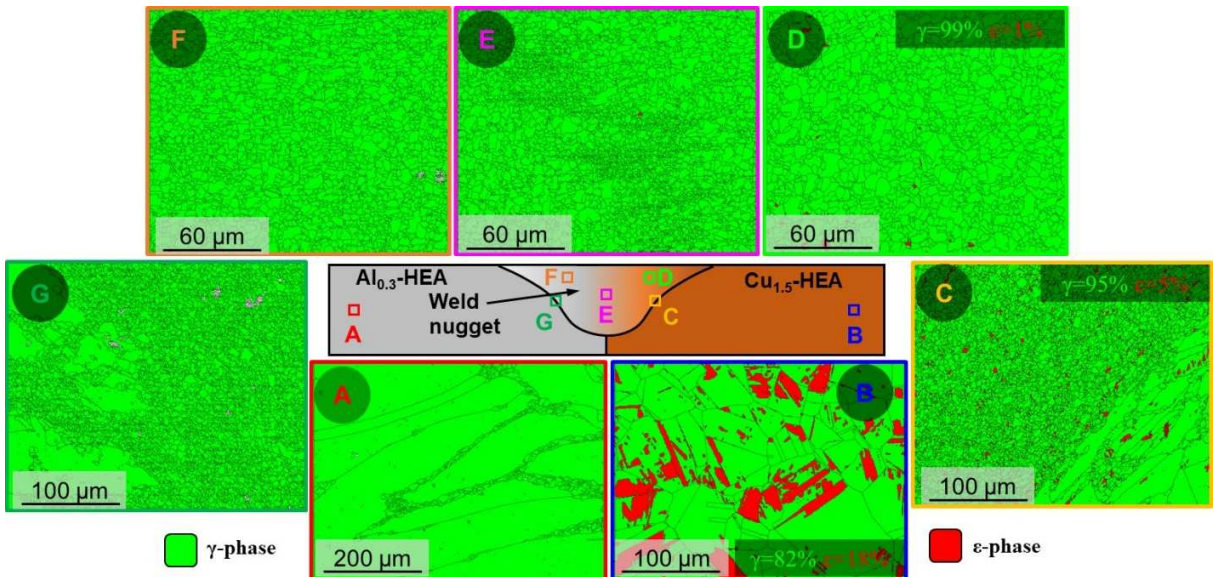


Figure 4: Phase maps obtained at multiple locations along the dissimilar weld of Al_{0.3} HEA and Cu_{1.5} HEA. (a) Base Al_{0.3} HEA, (b) base Cu_{1.5} HEA, (c) transition zone Al_{0.3} HEA, (d) SZ Cu_{1.5} HEA, (e) dissimilar weld line, (f) SZ Al_{0.3} HEA, and (g) transition zone Al_{0.3} HEA.

The influence of starting microstructure on the processed microstructure is governed by the fact that Al_{0.3} HEA is a single-phase HEA with a partially recrystallized microstructure, and

$\text{Cu}_{1.5}$ -HEA is a dual-phase TRIP HEA with low stacking fault energy (SFE) [20,30]. Furthermore, competition of recrystallization and transformation mechanisms during sustained high-temperature shear deformation also dictate the final microstructure in low SFE TRIP HEA after thermomechanical processing [31]. Notably, FSW of $\text{Cu}_{1.5}$ HEA resulted in a γ (f.c.c.)-dominant microstructure (99%) as compared to the initial dual phase microstructure of the base material, as thermomechanical processing aided γ (f.c.c.) phase stability, thus creating a larger volume fraction of γ (f.c.c.) phase available for transformation (Fig 4 (d)). Also, the ϵ (h.c.p) phase fraction in $\text{Cu}_{1.5}$ HEA gradually reduced when moved from base material (18%) (Fig. 4 (b)) to transition zone (5%) (Fig. 4 (c)) and then to SZ (1%) (Fig. 4 (d)). Such a difference in phase fraction is attributed to the spatial variation in strain, strain rate, and temperature in the nugget zone, all of which impact phase stability and recrystallization kinetics of the alloy [28,32]. The image taken along the weld lines (Figs. 3 (e) and 4 (e)) clearly revealed a very fine-grained microstructure band that is marked between the dashed lines (Fig. 3 (e)). The bimodal microstructure after FSW, where some larger grains are surrounded by finer recrystallized grains in both $\text{Al}_{0.3}$ HEA (Fig. 3 (f)) and $\text{Cu}_{1.5}$ HEA (Fig. 3 (d)), is due to multiple dynamic recrystallization and grain growth cycles that occurred as a result of sustained deformation at high temperature. Synergistic activity of strain, strain rate, and temperature during FSP allowed recrystallization of certain grains; whereas insufficient thermal energy restricted recrystallization in certain other grains, which appeared as larger grains with internal sub-cell formation. Recently, Agrawal et al. [31] reported the difference in transformation kinetics in newly recrystallized grains and grown grains in another low SFE $\text{Fe}_{40}\text{Co}_{20}\text{Mn}_{20}\text{Cr}_{15}\text{Si}_5$ TRIP HEA, where grown grains transformed to ϵ (h.c.p) phase; whereas newly-recrystallized grains endured as γ (f.c.c.) phase and correlated the observation to the dynamic dependence of SFE on grain size due to additional back stresses from grain boundaries. However, such a variation in transformation kinetics is not observed in $\text{Cu}_{1.5}$ HEA, as the addition of Cu stabilized the metastable γ (f.c.c.) phase, thereby inhibiting transformation during cooling [20].

The BSED image taken at the weld line (Fig. 5 (a)) reveals lack of any major defects and, hence, indicates strong bonding between the two alloys after welding. Figures 5 (b–i) show the EDS elemental maps corresponding to Fig. 5 (a). The maps give an indication of elemental diffusion from lean to rich regions across the weld line indicated by the variation in contrast. For example, the EDS maps of Mn (Fig. 5 (c)) and Si (Fig. 5 (g)) show contrast variation across the

weld line from the Mn- and Si-rich Cu_{1.5} HEA side to the lean Al_{0.3} HEA side. Also, BSED images towards the bottom of SZ (Fig. 5 (j)) indicated W and Re segregation (Figs. 5 (k) and (l)) due to tool wear during the welding process. However, such segregation did not have any detrimental effect on weld efficiency and mechanical properties which will be discussed in the next section.

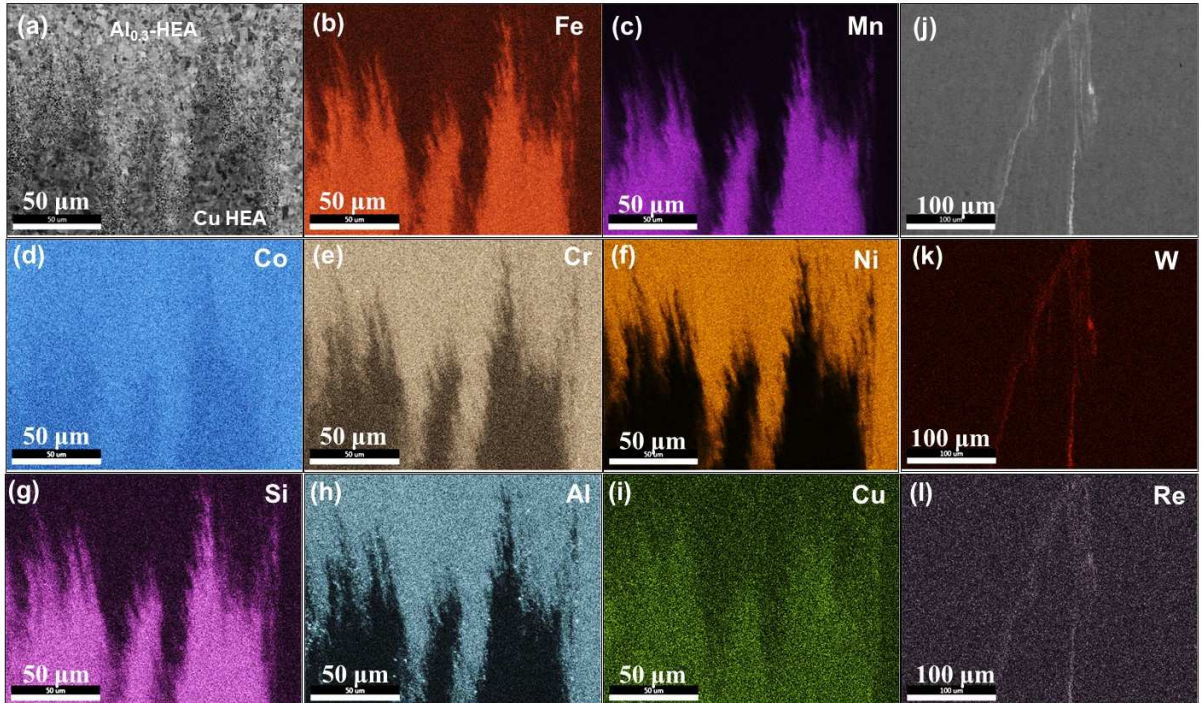


Figure 5: (a) BSED image along the weld line of the dissimilar weld, (b-i) EDS maps showing the elemental distribution along the weld line, (c) BSED image showing elemental segregation in the SZ which was revealed to be (k) W-rich and (l) Re-rich regions.

4.2 Mechanical Characterization

Figure 6 (a) shows the engineering stress-strain response of mini-tensile samples A–E milled out from multiple locations on the welded plates (Fig. 2 (a)). Cu_{1.5} HEA base material (sample D) had yield strength (YS) of 348 MPa and ultimate tensile strength (UTS) of 729 MPa, whereas Al_{0.3} HEA base material (sample A) yielded at 573 MPa with UTS of 732 MPa. Also, Cu_{1.5} HEA (49%) had higher failure strain than Al_{0.3} HEA (40%). The strain corresponding to the onset of instability during tensile deformation is identified by Considere's criterion, which is obtained by equating the strain hardening rate to true stress. Beyond Considere's strain (ε_c), strain localization associated with non-uniform deformation leads to necking and subsequent failure. Notably, Cu_{1.5} HEA failed with minimal non-uniform ductility ($\varepsilon_f - \varepsilon_c \sim 2\%$), whereas Al_{0.3} HEA

failed after considerable necking ($\varepsilon_f - \varepsilon_c \sim 16\%$). Good non-uniform ductility is beneficial especially in toughness limiting design instances, which assist in arresting the propagating crack front via crack blunting [33]. Figure 6 (b) shows the true stress-strain response (solid curves) and work hardening response (dashed curves) of samples A–E. Work hardening curves that correspond to samples A and D indicate a higher work hardening rate for Cu_{1.5} HEA base material (sample D) compared to Al_{0.3} HEA (sample A) in the uniform deformation regime. Additionally, the work hardening response of Cu_{1.5} HEA indicated a sustained hardening phase. Hence, Al_{0.3} HEA is characterized by good strength, reasonable hardening, and excellent non-uniform ductility; whereas Cu_{1.5} HEA is characterized by good strength, ductility, and excellent work hardening. Tensile tests performed on the mini-tensile sample extracted from the welded region of Al_{0.3} HEA (sample B) indicated an improved YS of 583 MPa and a UTS of 793 MPa compared to the base material, whereas the failure strain was reduced to 28%. Improvement in strength is attributed to Hall-Petch strengthening due to grain refinement following the welding. Similarly, YS and UTS for Cu_{1.5} HEA (sample C) after FSW improved to 480 MPa and 926 MPa, respectively, and ductility was improved to 62%. Rather, the work hardening responses of samples B and C are of interest. Figure 6 (b) indicates that the work hardening response of both as-processed materials has improved considerably compared to the base material post welding. To conclude, dissimilar friction stir welding improved the mechanical properties of both alloys. However, to establish weld efficiency and to determine the mechanical properties across the weld, a mini-tensile sample was milled out across the weld (sample E). Sample E showed YS of 562 MPa, UTS of 907 MPa, and 47% failure strain. The sample showed decent non-uniform ductility ($\varepsilon_f - \varepsilon_c \sim 6.5\%$) as well. The work hardening response of sample E was obtained higher than sample B (Al_{0.3} HEA (FSW)) and almost reached the work hardening rate of sample C (Cu_{1.5} HEA (FSW)) (Fig. 6 (b)). Hence, tensile stress-strain response of sample E blended the worthy aspects of both materials; viz., strength, work hardening, uniform ductility, as well as non-uniform elongation post necking. Figure 6 (c) shows hardness mapping along the lines A-A', B-B', C-C', and D-D' across the weld (6 (d) schematic). The profiles clearly indicate an increase in hardness in the welded region compared to the base material. Hardness improvement is more pronounced in Cu_{1.5} HEA than in Al_{0.3} HEA.

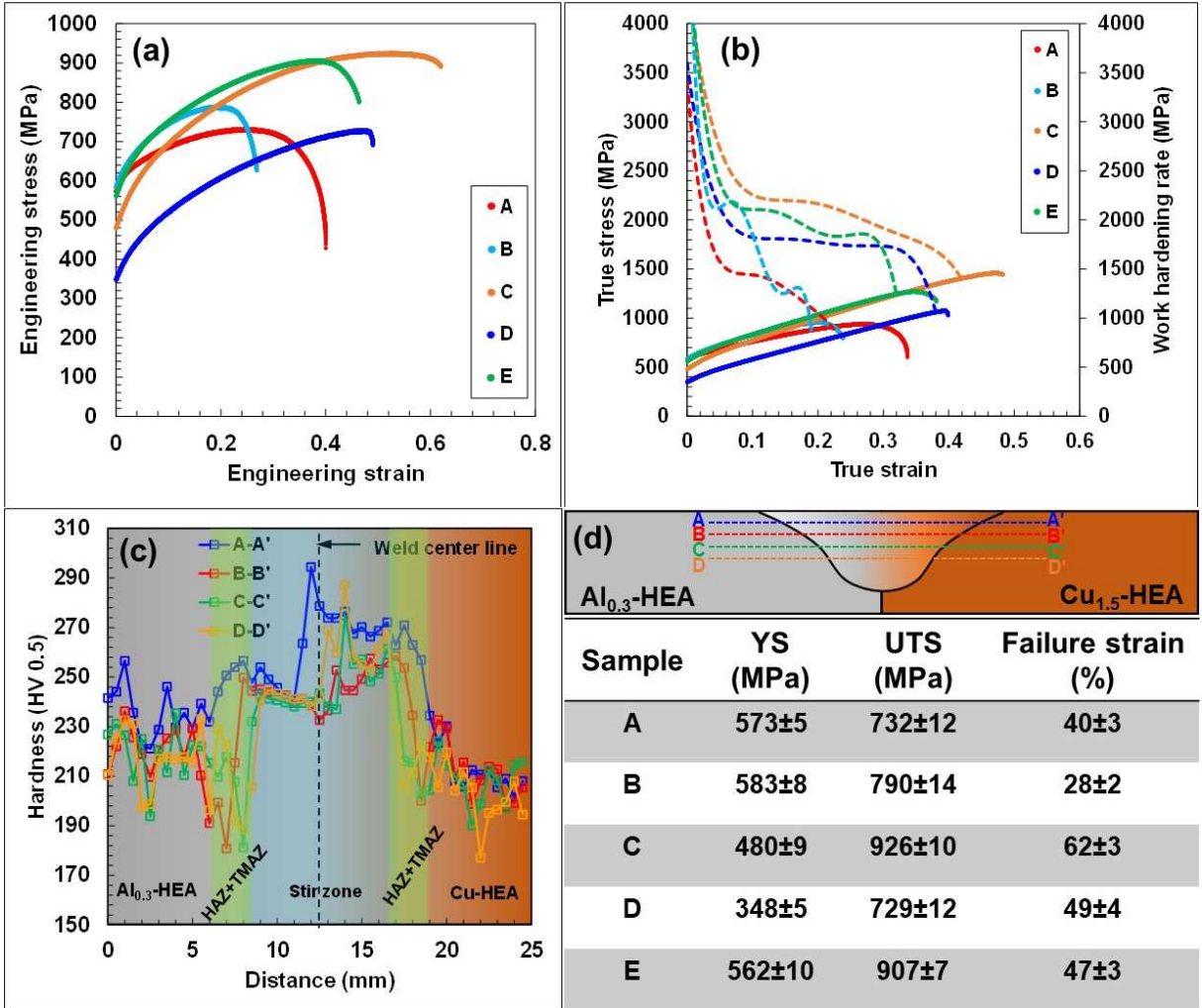


Figure 6: (a) Engineering stress-strain response of samples A-E indicated in Fig. 2 (a), (b) true stress-true strain (solid curves) and work hardening rate responses (dashed curves) of samples A-E, and (c) Vickers hardness profiles obtained along the segments shown in the schematic in (d).

The work hardening response of materials exhibiting transformation induced plasticity (TRIP) and twinning induced plasticity (TWIP) can be divided into three stages [34,35]: Stage I corresponds to a drop in work hardening rate; Stage II is characterized by a constant/increase in work hardening rate; and Stage III is accompanied by a drop in work hardening rate, which subsequently leads to fracture. In general, the magnitude of the work hardening rate during Stage II deformation of Al_{0.3} HEA turned out to be lower than Cu_{1.5} HEA (Fig. (6 (b))) in both as-received and FSP conditions. The sustained work hardening rate during Stage II deformation is attributed to the activation of additional deformation mechanisms such as deformation twinning/martensitic transformation [36]. Additionally, the magnitude of the work hardening rate

in Stage II of deformation as correlated to the stacking fault energy (SFE) through an inverse power law regression fit suggests an increase in work hardening rate with reduction in SFE [34]. Various experimental studies on steels revealed that deformation twinning is probable for SFE values $>18 \text{ mJ m}^{-2}$ and $<30 \text{ mJ m}^{-2}$, whereas martensitic transformation is observed when SFE $<18 \text{ mJ m}^{-2}$. Kumar et al. [37] asserted that an SFE $<30 \text{ mJ m}^{-2}$ for Al_x HEA is due to addition of Al to CoCrFeNi quaternary alloy; whereas density functional theory calculations suggested SFE value of 35.2 mJ m^{-2} for $\text{Al}_{0.3}$ HEA [38], intimating the possibility of deformation twinning. Experimental studies have shown the propensity of deformation twinning in $\text{Al}_{0.3}$ HEA [39–42] after cold rolling, high strain rates, and cryogenic temperatures. However, rarely is deformation twinning under quasi-static loading conditions in $\text{Al}_{0.3}$ HEA observed where the deformation is accommodated majorly by slip-dominant dislocation activity [40,43]. On the other hand, persistent γ (f.c.c.) $\rightarrow\epsilon$ (h.c.p) martensitic transformation in $\text{Cu}_{1.5}$ HEA at all strain rates [30] resulted in excellent work hardening and ductility. Additionally, the SFE value of $\text{Cu}_{1.5}$ HEA was suggested to be $<10 \text{ mJ m}^{-2}$ [34]. Hence, the higher work hardening rate for $\text{Cu}_{1.5}$ HEA is attributed to γ (f.c.c.) $\rightarrow\epsilon$ (h.c.p) martensitic transformation during deformation as opposed to slip-dominant activity in $\text{Al}_{0.3}$ HEA.

5 Discussion

5.1 Deformation mechanisms

The addition of Al to CoCrFeNi quaternary alloy system was reported to reduce the SFE of the alloy [37]. With increase in Al content, the intrinsic SFE decrease [38] is in line with the realization that Al addition reduced the SFE of Cu and hence promoted additional deformation mechanisms when deformed [44]. As the Al content was varied from 2 wt.% to 6 wt.%, deformation twinning was observed as an additional strain accommodating mechanism. Similarly, by virtue of low SFE, $\text{Al}_x\text{CoCrFeNi}$ undergoes deformation twinning in specific compositions and loading conditions, and hence results in good ductility [39–42,45]. For example, $\text{Al}_{0.1}\text{CoCrFeNi}$ HEA deformed via normal {111} <011> planar dislocation glide activity at room temperature [46], whereas an increase in Al content in $\text{Al}_{0.5}\text{CoCrFeNi}$ HEA promoted deformation twinning at room temperature [45]. Specifically, $\text{Al}_{0.3}$ HEA showed deformation twinning in cold-rolled condition [39], high strain rate loading [41], and at cryogenic temperature [42]. However, $\text{Al}_{0.3}$ HEA did not exhibit any evidence of deformation

twinning at room temperature when deformed at quasi-static conditions, where the deformation mechanism was planar slip dominated [40,43]. Good ductility exhibited by the alloy at room temperature is attributed to persistent planar slip activity during deformation [42]. However, the decent work hardening exhibited in Al_{0.3} HEA in quasi-static loading condition was attributed to the dense dislocation tangle network in the microstructure [40]. Figure 7 (a1) shows the IPF map obtained from Al_{0.3} HEA (sample B) after failure near the fractured surface. Kernel Average Misorientation (KAM) map reveals the extent of deformation accommodated in the sample before failure (Fig. 7 (a2)) with an overall higher KAM value. There was no primary evidence of deformation modes other than dislocation dominated slip activity in the microstructure. The CSL Σ_3 twin boundaries in the deformed microstructure (Fig. 7 (a3)) were the pre-existing annealing twins in the microstructure after dynamic recrystallization rather than deformation twinning; all are discussed in a later section. Hence, the decent hardening showed by the alloy (Fig. 6 (b)) is due to the dense dislocation network present in the microstructure when deformed.

Following the alloy design strategy that introduced TRIP in HEAs [47], multiple alloys have been designed to invoke martensitic transformation via metastability engineering by addition of minor alloying elements such as Si, Al, and Cu [32]. The majority of the alloys exhibited γ (f.c.c.) $\rightarrow\epsilon$ (h.c.p) martensitic transformation under deformation [48]. Further refinement of alloy composition enabled γ (f.c.c.) $\rightarrow\epsilon$ (h.c.p) $\rightarrow\alpha$ (b.c.c.) martensitic transformation [49], thereby completing the Burger's transformation triangle [28]. The addition of 1.5 at.% Cu to Fe₄₀Mn₂₀Co₂₀Cr₁₅Si₅ HEA at the expense of Fe stabilized the metastable γ (f.c.c.) phase subjected to thermomechanical processing [20]. The alloy exhibited good synergy of strength, ductility, and work hardening owing to persistent γ (f.c.c.) $\rightarrow\epsilon$ (h.c.p.) martensitic transformation. Deformation in the transformed ϵ (h.c.p) through non-basal slip activity and deformation twinning supplemented the work hardening ability of the alloy and ductility [50,51]. Deformation initiates from slip and deformation twinning in the γ (f.c.c.) phase, and subsequently progresses to stacking fault formation and ϵ (h.c.p.) martensitic transformation [35]. Further deformation results in basal slip activity in the transformed ϵ (h.c.p.) martensitic phase, which later progresses through non-basal slip activity with change in c/a ratio and deformation twinning [50–52]. Such richness in deformation mechanisms in both phases in TRIP HEAs guaranteed excellent mechanical properties.

Figures 7 (b1 and b2) are the IPF map and phase map of Cu_{1.5} HEA (sample C) after tensile failure obtained near the failure surface. Evidently, the microstructure of the ϵ (h.c.p) dominant microstructure (80% ϵ) as opposed to the γ (f.c.c.)-dominant (99% γ) processed microstructure (Fig. 4 (d)) indicates the deformation-induced martensitic transformation achieved during deformation. Extension twinning widely reported in Mg alloys is characterized by a misorientation angle of $\sim 86^\circ$ [53–55]. Extension twinning improved work hardening and ductility in Mg alloys [56]. A neutron diffraction study performed on Fe₄₀Mn₂₀Co₂₀Cr₁₅Si₅ TRIP HEA revealed the presence of {10 $\bar{1}$ 2}{10 $\bar{1}$ 1} extension twinning as well as {10 $\bar{1}$ 1}{10 $\bar{1}$ 2} and {10 $\bar{1}$ 3}{30 $\bar{3}$ 2} type compression twinning in the ϵ (h.c.p) phase when subjected to tensile deformation [51]. The extension twins were characterized by a misorientation angle of $\sim 86.2^\circ$ in Fe₄₀Mn₂₀Co₂₀Cr₁₅Si₅ TRIP HEA, whereas the {10 $\bar{1}$ 1}{10 $\bar{1}$ 2} and {10 $\bar{1}$ 3}{30 $\bar{3}$ 2} type contraction twins were characterized by misorientation angles of $\sim 56^\circ$ and 64° , respectively [51]. Similar extension twinning was also observed in preferentially oriented grains in Cu_{1.5} HEA when subjected to high strain rate compressive loading [30]. Likewise, evidence of {10 $\bar{1}$ 2}{10 $\bar{1}$ 1} extension twinning and {10 $\bar{1}$ 3}{30 $\bar{3}$ 2} contraction twinning in the ϵ (h.c.p) phase of the deformed microstructure of Cu_{1.5} HEA was indicated by the rectangles in Fig. 7 (b1). Figures 7 (c1–c4) depict the enlarged area of the representative twins indicated in Fig. 7 (b1). Figures 7 (c1 and c2) are instances of {10 $\bar{1}$ 3}{30 $\bar{3}$ 2} contraction twins characterized by a misorientation angle of $\sim 64^\circ$ (Fig. 7 (d)), whereas Figs. 7 (c3 and c4) are instances of {10 $\bar{1}$ 2}{10 $\bar{1}$ 1} extension twins characterized by a misorientation angle of $\sim 86^\circ$ (Fig. 7 (e)). Hence, the excellent work hardening and ductility achieved in Cu_{1.5} HEA are attributed to multiple deformation mechanisms activated in both γ (f.c.c.) and ϵ (h.c.p) phases in addition to persistent martensitic transformation, which is the major deformation accommodation mechanism.

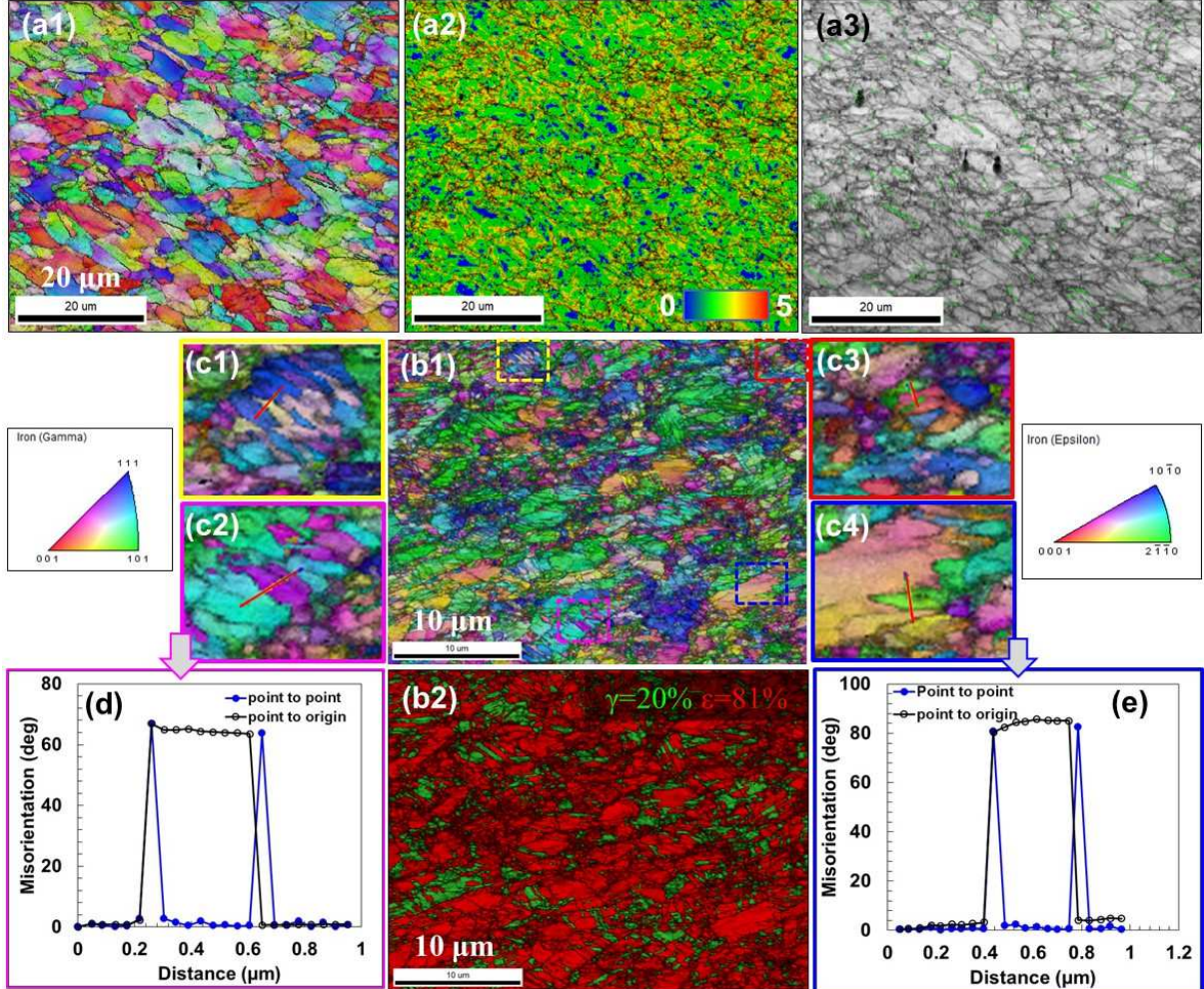


Figure 7: EBSD micrographs obtained near the fracture surface of Al_{0.3} HEA (a1) IPF map, (a2) KAM map, and (a3) misorientation map showing CSL Σ3 twin boundaries. EBSD micrographs obtained near the fracture surface of Cu_{1.5} HEA (b1) IPF map, (b2) phase map, (c1-c2) {10̄13}{30̄32} contraction twins, (c3-c4) {10̄12}{10̄11} extension twins present in Cu_{1.5} HEA martensitic phase, (d) misorientation profile across the twin in (c2), and (e) misorientation profile across the twin in (c4).

5.2 Dynamic recrystallization

Being a thermomechanical process, synergy of high strain, strain rate, and temperature causes the material to undergo the process of dynamic recrystallization (DRX) during FSW in order to reduce the free energy of the system and thereby result in the formation of newly-recrystallized, strain-free grains [57]. However, the method of dynamic recrystallization depends on the active dynamic recovery mechanism (DRV), which in turn depends on SFE of the material. High SFE materials undergo continuous dynamic recrystallization (CDRX) where newly recrystallized

grains are formed by sub-cell formation and grain boundary rotation. Low SFE materials undergo discontinuous dynamic recrystallization (DDRX), which is characterized by bulging of grain boundary and nucleation of newly recrystallized grains along the grain boundaries, and which grows at the expense of large deformed grains [58]. Figure 8 (a) shows the IPF map at the interface of the SZ and the base material of Cu_{1.5} HEA; Fig. 8 (b) presents the corresponding KAM map. The level of grain refinement and low KAM value in the SZ as compared to the base material indicate the recrystallization achieved during FSW and a strain-free microstructure in SZ.

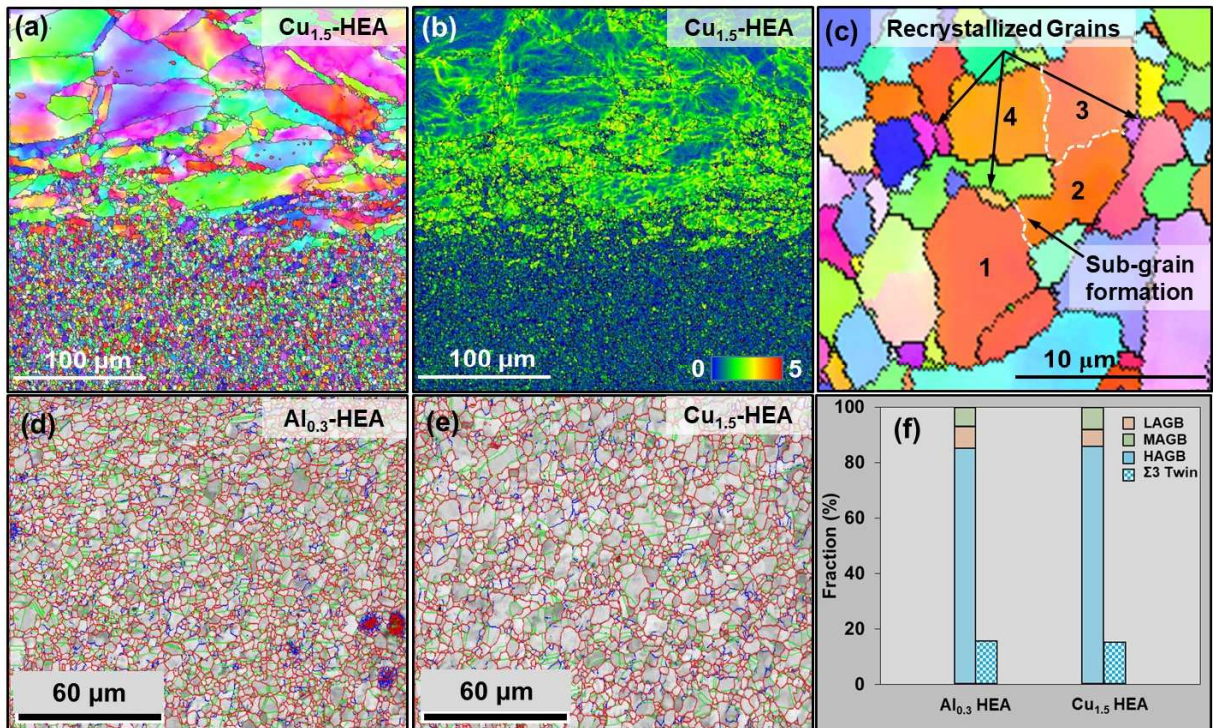


Figure 8: (a) IPF map obtained at the transition zone between the SZ and base material in Cu_{1.5} HEA, (b) KAM map corresponding to (a), (c) IPF map indicating sub-grain boundary formation within a grain in Cu_{1.5} HEA, grain boundary misorientation profile indicating the nature of grain boundaries in (d) Al_{0.3} HEA and (e) Cu_{1.5} HEA, and (f) percentage fraction of different grain boundaries in both Al_{0.3} HEA and Cu_{1.5} HEA.

Both Al_{0.3} HEA (~30 mJ m⁻²) and Cu_{1.5} HEA (~10 mJ m⁻²) were reported to have low SFE. A major deformation accommodation mechanism at room temperature is planar slip glide in Al_{0.3} HEA, whereas martensitic transformation occurs in Cu_{1.5} HEA. Patnamsetty et al. [59] studied the dynamic recrystallization mechanism during hot deformation of Al_{0.3} HEA as a function of

temperature and strain rate, and observed DDRX as the dominant DRX mechanism. Also, the recrystallized grain size increased with increase in temperature and reduced with strain rate. Haghdadi et al. [60] revealed the importance of micro-shear bands (MSB) as nucleation sites for recrystallization in addition to pre-existing grain boundaries. Formation of such recrystallized grains from MSBs is attributed to sub-grain rotation at lower strain levels. Figure 8 (d) shows grain boundary misorientation (θ) contrast profiles in the SZ of $\text{Al}_{0.3}$ HEA corresponding to the IPF map presented in Fig 3 (f). Red profiles indicate high angle grain boundaries (HAGB) ($15^\circ < \theta < 180^\circ$), whereas black and blue profiles indicate low angle grain boundaries (LAGB) ($1^\circ < \theta < 5^\circ$) and medium angle grain boundaries (MAGB) ($5^\circ < \theta < 15^\circ$), respectively. The CSL $\Sigma 3$ twin boundaries ($\theta = 60^\circ/(111)$) in the DRX microstructure are depicted in green color. Similarly, Fig. 8 (e) displays the grain boundary misorientation contrast profile for $\text{Cu}_{1.5}$ TRIP HEA. Figure 8 (f) shows the percentage length fraction of the various types of grain boundaries for both alloys. Larger volume fraction of HAGBs in the recrystallized microstructure of both $\text{Al}_{0.3}$ HEA (85%) and $\text{Cu}_{1.5}$ HEA (85.5%) suggests the DRX mechanism to be predominantly DDRX. Formation of HAGBs in low SFE materials is attributed to strain induced grain boundary (SIGB) migration due to lack of recovery mechanisms. Additionally, large fractions of $\Sigma 3$ twin boundaries were also observed in the microstructure of both alloys after welding; 16.2% in $\text{Al}_{0.3}$ HEA and 15.7% in $\text{Cu}_{1.5}$ HEA. Formation of $\Sigma 3$ twin boundaries is also a signature of DDRX that occurs after completion of SIGB migration, and results in the formation of a twin boundary [58]. However, signs of CDRX are also observed in the recrystallized microstructure of both HEAs, although small in fraction, indicated by the LAGBs in the microstructure. Figure 8 (c) specifies a representative grain in $\text{Cu}_{1.5}$ HEA and includes low-angled sub-grains (marked 1-4) revealing CDRX activity as well. CDRX is expected to occur in all materials irrespective of SFE [58]. Instances of CRDX in the microstructure could be attributed to temperature variations during ramping and cooling stages of FSW. To conclude, the mechanism of DRX is dominated predominantly by DDRX mechanism in both HEAs along with minor CDRX contribution.

5.3 Progression of deformation and weld efficiency

A primary advantage of FSW is the better mechanical property in the weldment compared to the base material in alloys such as stainless steel [61,62], nickel-based super alloys [63], and HEAs [27]. Such materials are reported to have 100% weld efficiency, which resulted in structural failure in the base material rather than in the welded region when pulled in tension.

Although the hardness profile for the current dissimilar weld indicated a stronger weld compared to the base material (Fig. 6 (c)), the progression of deformation in both alloys is of interest due to the difference in strength and work hardening characteristics. A sub-sized ASTM E8 sample taken across the weld was used for the study (Fig. 2 (a)). Figure 9 (a) shows the load-deformation response of the sample pulled in tension. Figure 9 (b) displays the real-time DIC axial strain maps corresponding to deformation levels as indicated by markers A–H in Fig. 9 (a). Clearly, the deformation initiated in Cu_{1.5} HEA base material during the primary phase of tensile deformation (marker B) is attributed to its lower YS (Fig. 6 (a)). Both Al_{0.3} HEA base material and the weld region remained undeformed during the initial deformation phase. With increase in strain, Cu_{1.5} HEA work hardens at a higher rate than Al_{0.3} HEA and results in an improvement in strength (Fig. 6 (b)). At point D, strain localization in the TMAZ/HAZ on the Al_{0.3} HEA side due to marginally low hardness as compared to Al_{0.3} HEA base material indicates the transfer of straining from Cu_{1.5} HEA side to Al_{0.3} HEA. Also, Al_{0.3} HEA base material started deforming, although the deformation rate is less compared to the Cu_{1.5} HEA base material. Subsequently, strain localization intensified in TMAZ/HAZ of Al_{0.3} HEA with concurrent deformation in both base materials, though at different rates. However, major deformation was still accommodated in Cu_{1.5} HEA base material during the uniform deformation segment from points D–F in the load-deformation graph. With deformation, Cu_{1.5} HEA base material work hardened to become stronger than its Al_{0.3} HEA counterpart (Fig. 6 (a)). Subsequently, at point F, Al_{0.3} HEA base material became the weakest region in the gage section, and started accommodating the major deformation, which subsequently led to necking and failure (marker H, Fig. 9 (a, b)) after containing the non-uniform deformation. Importantly, the weld nugget remained almost undeformed during the entire deformation regime, where the maximum axial strain at failure was determined to be less than 6% (Fig. 9 (b)), and indicated a weld of 100% efficiency. Figure 9 (c) shows the image of the failed specimen where the weld nugget remained almost undeformed compared to both base material HEAs.

As mentioned in Section 4.2, the mechanical property attributes of both HEAs were different. Interestingly, the deformation response in Fig. 9 (a) indicates that the mechanical property across the weld combines the good attributes of both HEAs at their respective advantageous zones of deformation in addition to a 100% efficient weld. In the uniform elongation regime, the major deformation as accommodated in Cu_{1.5} HEA base material via persistent martensitic

transformation resulted in good work hardening; whereas the deformation shifted to Al_{0.3} HEA in the non-uniform deformation regime, thereby enabling excellent non-uniform ductility post necking. To conclude, the load-deformation response of the tensile sample across the weld revealed a 100% efficient weld and indicated a progression in deformation from the Cu_{1.5} HEA side to Al_{0.3} HEA side, thereby combining the favorable mechanical attributes of both alloys.

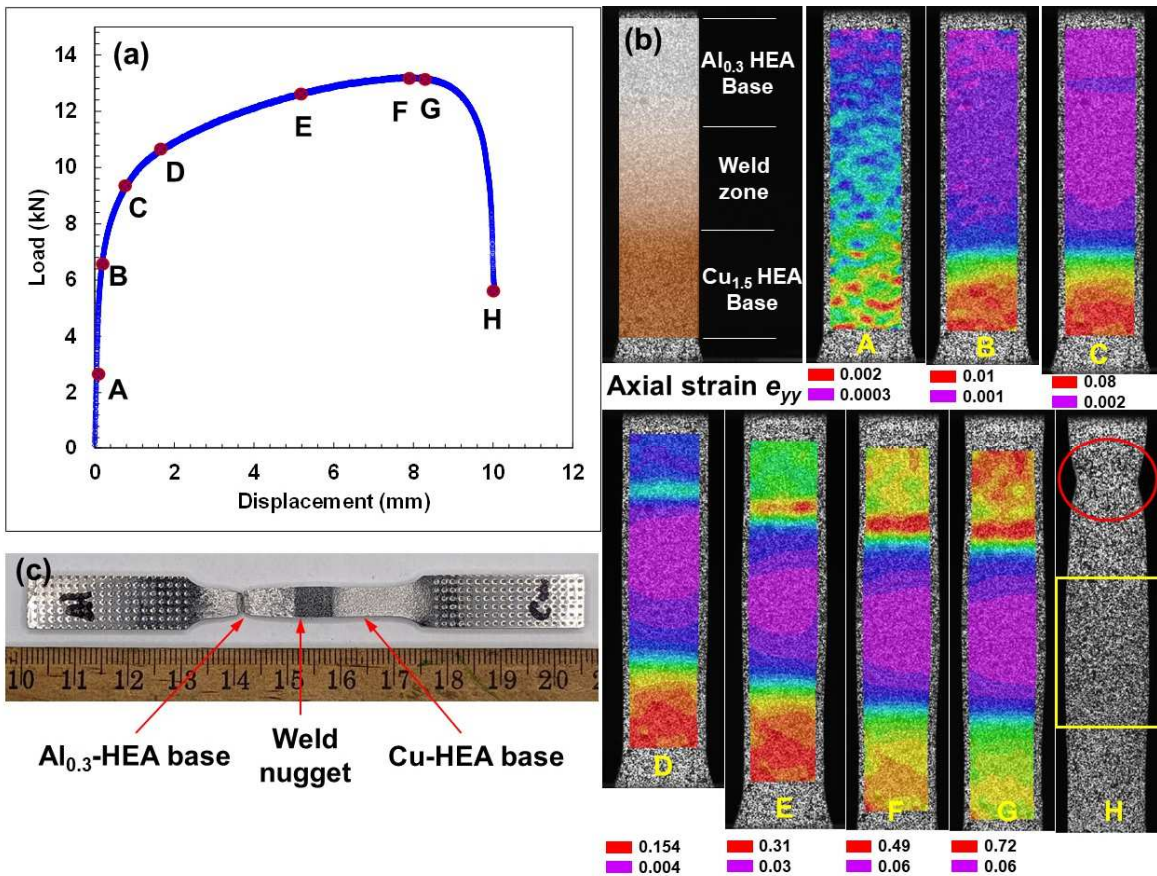


Figure 9: (a) Load-deformation response of tensile sample prepared across the weld, (a) real-time DIC strain mapping on the tensile sample corresponding to markers A–H in (a), and (c) image of the failed tensile sample.

5.4 Fractography

To understand the mode of failure, fractography was performed on all failed tensile samples (Fig. 10). A clean ductile failure with dimpled morphology was observed in all samples. However, the dimple morphology varied with processing conditions and the respective microstructure. Figure 10 (a) shows the fractured surface of Al_{0.3} HEA base material (sample A).

Evidently, the considerable reduction in the cross-section area (marked by yellow curves) was due to extended necking and non-uniform ductility. Uniform distribution of dimples on the fractured surface was observed on major portion of surface area (Fig. 10 (b1)). Additionally, a few stretched equiaxed dimples with central voids were also present at other sections (yellow arrows in Fig. 10 (b2)). Such large dimples suggest void nucleation as the failure initiation mechanism. Subsequently, the dimples grew with evolution of plastic deformation and, finally, adjacent dimples coalesced and led to final failure. Similarly, the fractograph of Cu_{1.5} HEA base material (sample D) (Fig. 10 (c-d)) indicates a ductile failure with uniform distribution of dimples. However, the fractured surface exhibited a discontinuous multi-faceted discontinuous morphology (facets indicated by yellow arrows in Fig. 10 (c)) and suggests inter-granular fracture in individual grains. An enlarged view of the fracture surface (Fig. 10 (d)) shows certain dimples with spherical particles at their nuclei (pink arrows), embedded in a network of fine dimples. The presence of such dimples with embedded globular particles indicates void nucleation in Cu_{1.5} HEA base material due to interfacial debonding. These particles could be Cu-rich particles as reported in a previous study [20]. However, lack of stretching of such particle-embedded dimples implies the incapability of the alloy to accommodate plastic flow under triaxial loading conditions. Additionally, the reduction in cross-sectional area at the fracture surface of Cu_{1.5} HEA (Fig. 10 (c)) not prominent as in Al_{0.3} HEA (Fig. 10 (a)) supplemented the lack of non-uniform deformation in tension (Fig. 6 (a)). Also, dimple size on the fracture surface in Cu_{1.5} HEA being much less than Al_{0.3} HEA (Figs. 6 (a, c)) suggested a lack of plastic flow and void growth post necking.

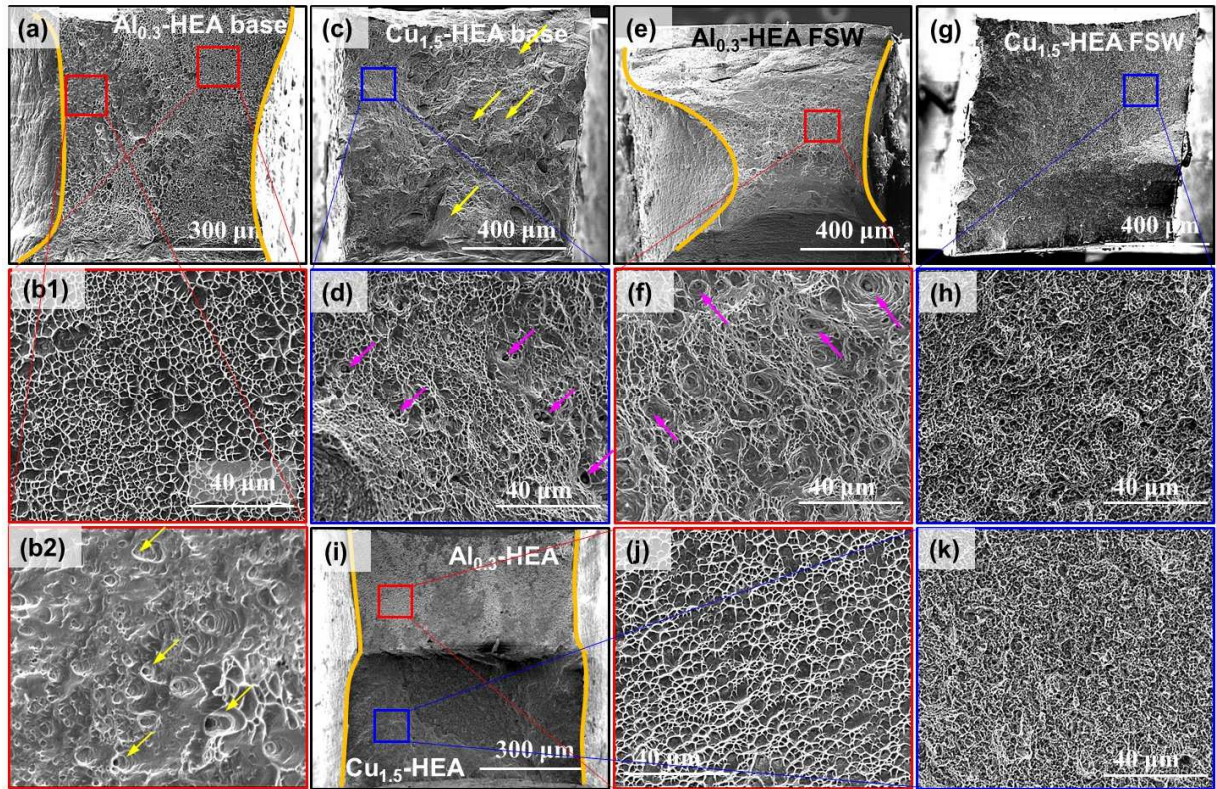


Figure 10: Fractograph of failed tensile samples, (a, b1, b2) $\text{Al}_{0.3}$ HEA base material, (c, d) $\text{Cu}_{1.5}$ HEA base material, (e, f) FSW $\text{Al}_{0.3}$ HEA, (g-h) FSW $\text{Cu}_{1.5}$ HEA, and (i, j, k) sample prepared across the weld (sample E in Fig. 2 (a)).

Figure 10 (e, f) show the fractured surface of FSW $\text{Al}_{0.3}$ HEA (sample B) after tensile deformation. The profuse reduction in cross-sectional area infers the capability of the alloy to sustain non-uniform ductility after FSW as well. An enlarged image of the fracture surface (Fig. 10 (f)) depicts randomly distributed stretched dimples (marked by pink arrows) among uniformly distributed fine dimples. The fracture mechanism clearly initiated with void nucleation, subsequent growth, coalescence, and failure. Very fine dimples compared to the base material is an additional indication of the level of grain refinement achieved after FSW. Similarly, Figs. 10 (g, h) show the fractography of FSW $\text{Cu}_{1.5}$ HEA sample (sample C) after tensile failure. Minimal reduction in cross-sectional area at the failure location indicates the lack of non-uniform ductility before failure. Also, a uniform distribution of extremely fine dimples was attributed to the presence of the refined microstructure. The fracture surface with no dimples with embedded particles (Fig. 10 (h)) suggests void nucleation not by particle debonding as opposed to $\text{Cu}_{1.5}$ HEA base material (Fig. 10 (d)). Figure 10 (i) presents the fractograph of sample E pulled across

the direction of the weld. As shown in Fig. 6 (a), the engineering stress-strain response integrated the favorable aspects of both alloys such as good work hardening, decent uniform ductility, and good non-uniform ductility as well. The sample would be expected to fail in the Al_{0.3} HEA section due to its low strength and ductility compared to its Cu_{1.5} HEA counterpart (Fig. 6(a)). However, fractograph (Fig. 10 (i)) characteristics of both Cu_{1.5} HEA and Al_{0.3} HEA confirm that the failure was not restricted to the weaker material. Clearly, larger area reduction in the Al_{0.3} HEA side compared to the Cu_{1.5} HEA side indicates the accommodation of non-uniform ductility by Al_{0.3} HEA. Also, Al_{0.3} HEA could sustain its strength during uniform elongation when the deformation was accommodated by Cu_{1.5} HEA. The expanded image of fracture surface on the Al_{0.3} HEA and Cu_{1.5} HEA sides presents characteristics similar to samples B and C, respectively. To conclude, excellent non-uniform ductility shown by Al_{0.3} HEA is attributed to the ability to sustain tri-axial plastic flow via growth of the voids, whereas the fracture surface of Cu_{1.5} HEA did not have any indication of dimple stretching and thus constricted plastic flow and non-uniform extension post necking.

6 Conclusions

Dissimilar welding of Al_{0.3} HEA and Cu_{1.5} TRIP HEA was performed using friction stir welding (FSW). A defect-free weld with a refined microstructure was obtained. Synergistic activity of strain and temperature resulted in a refined weld zone due to dynamic recrystallization. Detailed mechanical, microstructure, and fractography characterization was performed to understand weld performance. The following are important takeaways from the current study.

1. FSW of Al_{0.3} HEA and Cu_{1.5} TRIP HEA resulted in a strong weld with 100% weld efficiency.
2. Grain refinement achieved during FSW is attributed to the mechanism of discontinuous dynamic recrystallization (DDRX), which was revealed by the presence of a higher fraction of high angle grain boundaries (HAGBs) and CSL $\Sigma 3$ twin boundaries.
3. Tensile mechanical property across the weld showed integration of such favorable properties of both HEAs as excellent work hardening and ductility of Cu_{1.5} HEA and good non-uniform ductility of Al_{0.3} HEA.

4. Good work hardening rate achieved across the weld is attributed to persistent martensitic transformation and deformation twinning in Cu_{1.5} HEA. Non-uniform ductility is attributed to dislocation slip activity in Al_{0.3} HEA, which accommodated the tri-axial state of stress in the diffused necking zone.
5. Stretched voids on the fracture surface of Al_{0.3} HEA enabled the material to accommodate persistent plastic flow post-necking before failure, whereas voids on the fracture surface of Cu_{1.5} HEA were unstretched and thus limited non-uniform plastic deformation.

Acknowledgments

The present work was performed under the cooperative agreement between the Army Research Laboratory (ARL) and the University of North Texas (W911NF-18-2-0067). Authors acknowledge Materials Research Facility (MRF) at University of North Texas for access to scanning electron microscopy.

Data availability statement

The raw/processed data required to reproduce these findings cannot be shared at this time as the data also forms part of an ongoing study.

References

- [1] J.W. Yeh, S.K. Chen, S.J. Lin, J.Y. Gan, T.S. Chin, T.T. Shun, C.H. Tsau, S.Y. Chang, Nanostructured high-entropy alloys with multiple principal elements: Novel alloy design concepts and outcomes, *Adv. Eng. Mater.* 6 (2004) 299–303. <https://doi.org/10.1002/adem.200300567>.
- [2] Y. Zhang, T. Ting, Z. Tang, M.C. Gao, K.A. Dahmen, P.K. Liaw, Z. Ping, Progress in Materials Science Microstructures and properties of high-entropy alloys, *J. Prog. Mater. Sci.* 61 (2014) 1–93. <https://doi.org/10.1016/j.pmatsci.2013.10.001>.
- [3] J. Guo, C. Tang, G. Rothwell, L. Li, Y.-C. Wang, Q. Yang, X. Ren, Welding of High Entropy Alloys—A Review, *Entropy*. 21 (2019) 431. <https://doi.org/10.3390/e21040431>.
- [4] J.G. Lopes, J.P. Oliveira, A Short Review on Welding and Joining of High Entropy Alloys, *Metals (Basel)*. 10 (2020) 212. <https://doi.org/10.3390/met10020212>.
- [5] J. Li, X. Meng, L. Wan, Y. Huang, Welding of high entropy alloys: Progresses, challenges and perspectives, *J. Manuf. Process.* 68 (2021) 293–331. <https://doi.org/10.1016/j.jmapro.2021.05.042>.
- [6] J.P. Oliveira, J. Shen, Z. Zeng, J.M. Park, Y.T. Choi, N. Schell, E. Maawad, N. Zhou, H.S. Kim, Dissimilar laser welding of a CoCrFeMnNi high entropy alloy to 316 stainless steel, *Scr. Mater.* 206 (2022) 114219. <https://doi.org/10.1016/j.scriptamat.2021.114219>.
- [7] R. Sokkalingam, P. Mastanaiah, V. Muthupandi, K. Sivaprasad, K.G. Prashanth, Electron-

beam welding of high-entropy alloy and stainless steel: microstructure and mechanical properties, *Mater. Manuf. Process.* 35 (2020) 1885–1894. <https://doi.org/10.1080/10426914.2020.1802045>.

- [8] R. Sokkalingam, B. Pravallika, K. Sivaprasad, V. Muthupandi, K.G. Prashanth, Dissimilar welding of high-entropy alloy to Inconel 718 superalloy for structural applications, *J. Mater. Res.* 37 (2022) 272–283. <https://doi.org/10.1557/s43578-021-00352-w>.
- [9] A. Arab, Y. Guo, Q. Zhou, P. Chen, Joining AlCoCrFeNi high entropy alloys and Al-6061 by explosive welding method, *Vacuum.* 174 (2020) 109221. <https://doi.org/10.1016/j.vacuum.2020.109221>.
- [10] N.K. Adomako, G. Shin, N. Park, K. Park, J.H. Kim, Laser dissimilar welding of CoCrFeMnNi-high entropy alloy and duplex stainless steel, *J. Mater. Sci. Technol.* 85 (2021) 95–105. <https://doi.org/10.1016/j.jmst.2021.02.003>.
- [11] J.P. Oliveira, A. Shamsolhodaei, J. Shen, J.G. Lopes, R.M. Gonçalves, M. de Brito Ferraz, L. Piçarra, Z. Zeng, N. Schell, N. Zhou, H. Seop Kim, Improving the ductility in laser welded joints of CoCrFeMnNi high entropy alloy to 316 stainless steel, *Mater. Des.* 219 (2022) 110717. <https://doi.org/10.1016/j.matdes.2022.110717>.
- [12] B. Cantor, I.T.H. Chang, P. Knight, A.J.B. Vincent, Microstructural development in equiatomic multicomponent alloys, *Mater. Sci. Eng. A.* 375–377 (2004) 213–218. <https://doi.org/10.1016/j.msea.2003.10.257>.
- [13] Z. Li, K.G. Pradeep, Y. Deng, D. Raabe, C.C. Tasan, Metastable high-entropy dual-phase alloys overcome the strength-ductility trade-off, *Nature.* 534 (2016) 227–230. <https://doi.org/10.1038/nature17981>.
- [14] J.Y. He, H. Wang, H.L. Huang, X.D. Xu, M.W. Chen, Y. Wu, X.J. Liu, T.G. Nieh, K. An, Z.P. Lu, A precipitation-hardened high-entropy alloy with outstanding tensile properties, *Acta Mater.* 102 (2016) 187–196. <https://doi.org/10.1016/j.actamat.2015.08.076>.
- [15] B. Gwalani, S. Gorsse, D. Choudhuri, M. Styles, Y. Zheng, R.S. Mishra, R. Banerjee, Modifying transformation pathways in high entropy alloys or complex concentrated alloys via thermo-mechanical processing, *Acta Mater.* 153 (2018) 169–185. <https://doi.org/10.1016/j.actamat.2018.05.009>.
- [16] B. Gwalani, V. Soni, M. Lee, S.A. Mantri, Y. Ren, R. Banerjee, Optimizing the coupled effects of Hall-Petch and precipitation strengthening in a Al0.3CoCrFeNi high entropy alloy, *Mater. Des.* 121 (2017) 254–260. <https://doi.org/10.1016/j.matdes.2017.02.072>.
- [17] B. Gwalani, S. Gorsse, D. Choudhuri, Y. Zheng, R.S. Mishra, R. Banerjee, Tensile yield strength of a single bulk Al 0.3 CoCrFeNi high entropy alloy can be tuned from 160 MPa to 1800 MPa, *Scr. Mater.* 162 (2019) 18–23. <https://doi.org/10.1016/j.scriptamat.2018.10.023>.
- [18] K. Liu, M. Komarasamy, B. Gwalani, S. Shukla, R.S. Mishra, Fatigue behavior of ultrafine grained triplex Al0.3CoCrFeNi high entropy alloy, *Scr. Mater.* 158 (2019) 116–120. <https://doi.org/10.1016/j.scriptamat.2018.08.048>.
- [19] S. Muskeri, B. Gwalani, S. Jha, A. Yu, P.A. Jannotti, R.S. Haridas, B.E. Schuster, J.T. Lloyd, R.S. Mishra, S. Mukherjee, Excellent ballistic impact resistance of Al0.3CoCrFeNi

multi-principal element alloy with unique bimodal microstructure, *Sci. Rep.* 11 (2021) 1–12. <https://doi.org/10.1038/s41598-021-02209-y>.

- [20] S.S. Nene, M. Frank, K. Liu, S. Sinha, R.S. Mishra, B.A. McWilliams, K.C. Cho, Corrosion-resistant high entropy alloy with high strength and ductility, *Scr. Mater.* 166 (2019) 168–172. <https://doi.org/10.1016/J.SCRIPTAMAT.2019.03.028>.
- [21] K. Liu, S.S. Nene, M. Frank, S. Sinha, R.S. Mishra, Extremely high fatigue resistance in an ultrafine grained high entropy alloy, *Appl. Mater. Today.* 15 (2019) 525–530. <https://doi.org/10.1016/J.APMT.2019.04.001>.
- [22] M.-G. Jo, H.-J. Kim, M. Kang, P.P. Madakashira, E.S. Park, J.-Y. Suh, D.-I. Kim, S.-T. Hong, H.N. Han, Microstructure and mechanical properties of friction stir welded and laser welded high entropy alloy CrMnFeCoNi, *Met. Mater. Int.* 24 (2018) 73–83. <https://doi.org/10.1007/s12540-017-7248-x>.
- [23] D. Shaysultanov, N. Stepanov, S. Malopheyev, I. Vysotskiy, V. Sanin, S. Mironov, R. Kaibyshev, G. Salishchev, S. Zherebtsov, Friction stir welding of a carbon-doped CoCrFeNiMn high-entropy alloy, *Mater. Charact.* 145 (2018) 353–361. <https://doi.org/10.1016/j.matchar.2018.08.063>.
- [24] X. Qin, Y. Xu, Y. Sun, H. Fujii, Z. Zhu, C.H. Shek, Effect of process parameters on microstructure and mechanical properties of friction stir welded CoCrFeNi high entropy alloy, *Mater. Sci. Eng. A.* 782 (2020) 139277. <https://doi.org/10.1016/j.msea.2020.139277>.
- [25] P.-T. Lin, H.-C. Liu, P.-Y. Hsieh, C.-Y. Wei, C.-W. Tsai, Y.S. Sato, S.-C. Chen, H.-W. Yen, N.-H. Lu, C.-H. Chen, Heterogeneous structure-induced strength-ductility synergy by partial recrystallization during friction stir welding of a high-entropy alloy, *Mater. Des.* 197 (2021) 109238. <https://doi.org/10.1016/j.matdes.2020.109238>.
- [26] D. Shaysultanov, K. Raimov, N. Stepanov, S. Zherebtsov, Friction Stir Welding of a TRIP Fe49Mn30Cr10Co10C1 High Entropy Alloy, *Metals* (Basel). 11 (2020) 66. <https://doi.org/10.3390/met11010066>.
- [27] Z.G. Zhu, Y.F. Sun, M.H. Goh, F.L. Ng, Q.B. Nguyen, H. Fujii, S.M.L. Nai, J. Wei, C.H. Shek, Friction stir welding of a CoCrFeNiAl0.3 high entropy alloy, *Mater. Lett.* 205 (2017) 142–144. <https://doi.org/10.1016/j.matlet.2017.06.073>.
- [28] R.S. Mishra, R.S. Haridas, P. Agrawal, High entropy alloys – Tunability of deformation mechanisms through integration of compositional and microstructural domains, *Mater. Sci. Eng. A.* 812 (2021) 141085. <https://doi.org/10.1016/j.msea.2021.141085>.
- [29] ASTM E8, ASTM E8/E8M standard test methods for tension testing of metallic materials 1, Annu. B. ASTM Stand. 4. (2010) 1–27. <https://doi.org/10.1520/E0008>.
- [30] R.S. Haridas, P. Agrawal, S. Thapliyal, S. Yadav, Strain rate sensitive microstructural evolution in a TRIP assisted high entropy alloy: Experiments , microstructure and modeling, *Mech. Mater.* 156 (2021) 103798. <https://doi.org/10.1016/j.mechmat.2021.103798>.
- [31] P. Agrawal, R.S. Haridas, P. Agrawal, R.S. Mishra, Deformation based additive manufacturing of a metastable high entropy alloy via Additive friction stir deposition,

Addit. Manuf. 60 (2022) 103282. <https://doi.org/10.1016/j.addma.2022.103282>.

- [32] R.S. Mishra, S.S. Nene, M. Frank, S. Sinha, K. Liu, S. Shukla, Metastability driven hierarchical microstructural engineering: Overview of mechanical properties of metastable complex concentrated alloys, *J. Alloys Compd.* 842 (2020) 155625. <https://doi.org/10.1016/j.jallcom.2020.155625>.
- [33] S. Sinha, M. Komarasamy, T. Wang, R.S. Haridas, P. Agrawal, S. Shukla, S. Thapliyal, M. Frank, R.S. Mishra, Notch-tensile behavior of Al0.1CrFeCoNi high entropy alloy, *Mater. Sci. Eng. A.* 774 (2020) 138918. <https://doi.org/https://doi.org/10.1016/j.msea.2020.138918>.
- [34] R.S. Haridas, P. Agrawal, R.S. Mishra, Modeling the work hardening behavior in metastable high entropy alloys, *Mater. Sci. Eng. A.* 823 (2021) 141778. <https://doi.org/10.1016/j.msea.2021.141778>.
- [35] R.S. Haridas, P. Agrawal, S. Yadav, P. Agrawal, A. Gumaste, R.S. Mishra, Work hardening in metastable high entropy alloys: A modified five-parameter model, *J. Mater. Res. Technol.* 18 (2022) 3358–3372. <https://doi.org/10.1016/j.jmrt.2022.04.016>.
- [36] J.T. Lloyd, D.M. Field, K.R. Limmer, A four parameter hardening model for TWIP and TRIP steels, *Mater. Des.* 194 (2020). <https://doi.org/10.1016/j.matdes.2020.108878>.
- [37] N. Kumar, Q. Ying, X. Nie, R.S. Mishra, Z. Tang, P.K. Liaw, R.E. Brennan, K.J. Doherty, K.C. Cho, High strain-rate compressive deformation behavior of the Al0.1CrFeCoNi high entropy alloy, *Mater. Des.* 86 (2015) 598–602. <https://doi.org/10.1016/j.matdes.2015.07.161>.
- [38] M. Beyramali Kivy, M. Asle Zaeem, Generalized stacking fault energies, ductilities, and twinnabilities of CoCrFeNi-based face-centered cubic high entropy alloys, *Scr. Mater.* 139 (2017) 83–86. <https://doi.org/10.1016/j.scriptamat.2017.06.014>.
- [39] S. Dasari, A. Sarkar, A. Sharma, B. Gwalani, D. Choudhuri, V. Soni, S. Manda, I. Samajdar, R. Banerjee, Recovery of Cold-worked Al0.3CoCrFeNi Complex Concentrated Alloy through Twinning Assisted B2 Precipitation Resulting in Excellent Strength-Ductility Combination, *Acta Mater.* (2020). <https://doi.org/10.1016/j.actamat.2020.10.071>.
- [40] Z. Li, S. Zhao, H. Diao, P.K. Liaw, M.A. Meyers, High-velocity deformation of Al0.3CoCrFeNi high-entropy alloy: Remarkable resistance to shear failure, *Sci. Rep.* 7 (2017) 42742. <https://doi.org/10.1038/srep42742>.
- [41] S. Gangireddy, B. Gwalani, K. Liu, R. Banerjee, R.S. Mishra, Microstructures with extraordinary dynamic work hardening and strain rate sensitivity in Al0.3CoCrFeNi high entropy alloy, *Mater. Sci. Eng. A.* 734 (2018) 42–50. <https://doi.org/10.1016/j.msea.2018.07.088>.
- [42] I.V. Kireeva, Y.I. Chumlyakov, Z.V. Pobedennaya, A.V. Vyrodova, I.V. Kuksaguzen, D.A. Kuksaguzen, Orientation and temperature dependence of a planar slip and twinning in single crystals of Al0.3CoCrFeNi high-entropy alloy, *Mater. Sci. Eng. A.* 737 (2018) 47–60. <https://doi.org/10.1016/j.msea.2018.09.025>.
- [43] D. Li, C. Li, T. Feng, Y. Zhang, G. Sha, J.J. Lewandowski, P.K. Liaw, Y. Zhang, High-entropy Al0.3CoCrFeNi alloy fibers with high tensile strength and ductility at ambient and

cryogenic temperatures, *Acta Mater.* 123 (2017) 285–294.
<https://doi.org/10.1016/j.actamat.2016.10.038>.

- [44] A. Rohatgi, K.S. Vecchio, G.T. Gray, The influence of stacking fault energy on the mechanical behavior of Cu and Cu-al alloys: Deformation twinning, work hardening, and dynamic recovery, *Metall. Mater. Trans. A Phys. Metall. Mater. Sci.* 32 (2001) 135–145. <https://doi.org/10.1007/s11661-001-0109-7>.
- [45] M. Bönisch, Y. Wu, H. Sehitoglu, Twinning-induced strain hardening in dual-phase FeCoCrNiAl0.5 at room and cryogenic temperature, *Sci. Rep.* 8 (2018) 10663. <https://doi.org/10.1038/s41598-018-28784-1>.
- [46] S. Xia, Y. Zhang, Deformation mechanisms of Al0.1CoCrFeNi high entropy alloy at ambient and cryogenic temperatures, *Mater. Sci. Eng. A.* 733 (2018) 408–413. <https://doi.org/10.1016/j.msea.2018.07.073>.
- [47] Z. Li, K.G. Pradeep, Y. Deng, D. Raabe, C.C. Tasan, Metastable high-entropy dual-phase alloys overcome the strength–ductility trade-off, *Nature.* 534 (2016) 227–230. <https://doi.org/10.1038/nature17981>.
- [48] S.S. Nene, M. Frank, P. Agrawal, S. Sinha, K. Liu, S. Shukla, R.S. Mishra, B.A. McWilliams, K.C. Cho, Microstructurally flexible high entropy alloys: Linkages between alloy design and deformation behavior, *Mater. Des.* 194 (2020) 108968. <https://doi.org/10.1016/j.matdes.2020.108968>.
- [49] Y.H. Jo, J. Yang, W.-M. Choi, K.-Y. Doh, D. Lee, H.S. Kim, B.-J. Lee, S.S. Sohn, S. Lee, Body-centered-cubic martensite and the role on room-temperature tensile properties in Si-added SiVCrMnFeCo high-entropy alloys, *J. Mater. Sci. Technol.* 76 (2021) 222–230. <https://doi.org/10.1016/j.jmst.2020.10.038>.
- [50] S. Sinha, S.S. Nene, M. Frank, K. Liu, R.A. Lebensohn, R.S. Mishra, Deformation mechanisms and ductile fracture characteristics of a friction stir processed transformative high entropy alloy, *Acta Mater.* 184 (2020) 164–178. <https://doi.org/10.1016/j.actamat.2019.11.056>.
- [51] M. Frank, Y. Chen, S.S. Nene, S. Sinha, K. Liu, K. An, R.S. Mishra, Investigating the deformation mechanisms of a highly metastable high entropy alloy using in-situ neutron diffraction, *Mater. Today Commun.* 23 (2020) 100858. <https://doi.org/10.1016/J.MTCOMM.2019.100858>.
- [52] Y. Bu, Z. Li, J. Liu, H. Wang, D. Raabe, W. Yang, Nonbasal Slip Systems Enable a Strong and Ductile Hexagonal-Close-Packed High-Entropy Phase, *Phys. Rev. Lett.* 122 (2019) 75502. <https://doi.org/10.1103/PhysRevLett.122.075502>.
- [53] P. Chen, B. Li, D. Culbertson, Y. Jiang, Contribution of extension twinning to plastic strain at low stress stage deformation of a Mg-3Al-1Zn alloy, *Mater. Sci. Eng. A.* 709 (2018) 40–45. <https://doi.org/10.1016/j.msea.2017.10.038>.
- [54] H.J. Yang, S.M. Yin, C.X. Huang, Z.F. Zhang, S.D. Wu, S.X. Li, Y.D. Liu, EBSD Study on Deformation Twinning in AZ31 Magnesium Alloy During Quasi-in-Situ Compression, *Adv. Eng. Mater.* 10 (2008) 955–960. <https://doi.org/10.1002/adem.200800111>.
- [55] S.-G. Hong, S.H. Park, C.S. Lee, Role of {10–12} twinning characteristics in the

- deformation behavior of a polycrystalline magnesium alloy, *Acta Mater.* 58 (2010) 5873–5885. <https://doi.org/10.1016/j.actamat.2010.07.002>.
- [56] M.R. Barnett, Twinning and the ductility of magnesium alloys, *Mater. Sci. Eng. A.* 464 (2007) 1–7. <https://doi.org/10.1016/j.msea.2006.12.037>.
 - [57] R.S. Mishra, Z.Y. Ma, Friction stir welding and processing, *Mater. Sci. Eng. R Reports.* 50 (2005) 1–78. <https://doi.org/10.1016/j.mser.2005.07.001>.
 - [58] K. Huang, R.E. Logé, A review of dynamic recrystallization phenomena in metallic materials, *Mater. Des.* 111 (2016) 548–574. <https://doi.org/10.1016/j.matdes.2016.09.012>.
 - [59] M. Patnamsetty, S. Ghosh, M.C. Somani, P. Peura, Characterization of hot deformation behavior of Al0.3CoCrFeNi high-entropy alloy and development of processing map, *J. Alloys Compd.* 914 (2022) 165341. <https://doi.org/10.1016/j.jallcom.2022.165341>.
 - [60] N. Haghadi, S. Primig, M. Annasamy, P. Cizek, P.D. Hodgson, D.M. Fabijanic, On the hot-worked microstructure of a face-centered cubic Al0.3CoCrFeNi high entropy alloy, *Scr. Mater.* 178 (2020) 144–149. <https://doi.org/10.1016/j.scriptamat.2019.11.022>.
 - [61] H.-H. Cho, H.N. Han, S.-T. Hong, J.-H. Park, Y.-J. Kwon, S.-H. Kim, R.J. Steel, Microstructural analysis of friction stir welded ferritic stainless steel, *Mater. Sci. Eng. A.* 528 (2011) 2889–2894. <https://doi.org/10.1016/j.msea.2010.12.061>.
 - [62] A.N. Siddiquee, S. Pandey, N.Z. Khan, Friction Stir Welding of Austenitic Stainless Steel: A Study on Microstructure and Effect of Parameters on Tensile Strength, *Mater. Today Proc.* 2 (2015) 1388–1397. <https://doi.org/10.1016/j.matpr.2015.07.058>.
 - [63] K.H. Song, H. Fujii, K. Nakata, Effect of welding speed on microstructural and mechanical properties of friction stir welded Inconel 600, *Mater. Des.* 30 (2009) 3972–3978. <https://doi.org/10.1016/j.matdes.2009.05.033>.

